

Radial distribution functions of non-additive hard sphere mixtures via Percus' test particle route

Paul Hopkins¹ and Matthias Schmidt^{1,2}

¹ H H Wills Physics Laboratory, University of Bristol, Tyndall Avenue, Bristol BS8 1TL, UK

² Theoretische Physik II, Physikalisches Institut, Universität Bayreuth, D-95440 Bayreuth, Germany

Received 30 April 2011, in final form 17 June 2011

Published 21 July 2011

Online at stacks.iop.org/JPhysCM/23/325104

Abstract

Using fundamental density functional theory we calculate the partial radial distribution functions, $g_{ij}(r)$, of a binary non-additive hard sphere mixture using either Percus' test particle approach or inversion of the analytic structure factor obtained via the Ornstein–Zernike route. We find good agreement between the theoretical results and Monte Carlo simulation data for both positive and moderate negative non-additivities. We investigate the asymptotic, $r \rightarrow \infty$, decay of the $g_{ij}(r)$ and show that this agrees with the analytic analysis of the contributions to the partial structure factors in the plane of complex wavevectors. We find the test particle density profiles to be free of unphysical artefacts, contrary to earlier reports.

1. Introduction

The simple model of non-additive hard sphere (NAHS) mixtures has been shown to exhibit a rich phenomenology, including liquid–liquid demixing [1], crystallization, confinement driven population inversion [2–4], and striking wetting and layering behaviour at a general hard wall [5]. These transitions are all driven by excluded volume and hence entropy effects alone. NAHS mixtures constitute arguably one of the most fundamental liquid models to exhibit such behaviour. NAHSs can be used as a reference model in the study of more complex systems, such as alloys [6–8], colloids [9], electrolytes [10, 11], and polymers [12, 13].

Recent work has shown that the fundamental measure density functional theory (DFT) for binary NAHSs [14, 15] is a very suitable tool for the investigation of the above phenomena. The theory has been used to successfully describe (partial) radial distribution functions $g_{ij}(r)$ [14, 16], bulk fluid demixing phase diagrams [15], the structure and interfacial thermodynamics of the free fluid interface [15], as well as phenomena due to confinement in planar slits [4] and due to exposure to a planar wall [5]. Comparison to results from Monte Carlo simulations for bulk fluid–fluid phase diagrams, partial radial distribution functions and density profiles in planar slits indicates very good quantitative agreement. In this paper we re-address the problem of calculating $g_{ij}(r)$, in the

light of [15] and [16], with the aim of characterizing the bulk fluid structure.

Given a DFT approximation, the simplest way to obtain the $g_{ij}(r)$ is via numerical Fourier transform of the analytic structure factors. These are obtained from (analytic) direct correlation functions, which in turn can be directly obtained from the free energy functional via functional differentiation. The direct correlation functions are then inserted into the Ornstein–Zernike (OZ) equation to give partial structure factors and Fourier transforming to real space yields the $g_{ij}(r)$. Starting with the direct correlation functions, one can also transform the OZ equations into contour integrals in the complex plane, such that the radial distribution functions are expressed as a sum over the poles (divergences) of the analytic structure factors [17–20]. The advantage of this method is that it is possible to investigate individual contributions to the $g_{ij}(r)$, which either decay monotonically with distance or are damped oscillatory. In particular one can identify the contributions with the longest decay length; these determine the asymptotic (large distance) decay of the correlation functions in real space. It can be shown that the $g_{ij}(r)$ for all pairs of species ij exhibit a common asymptotic decay type and decay length and, in the oscillatory regime, a common wavelength. These properties of the asymptotic decay also determine the asymptotic (and often intermediate) decay of inhomogeneous density profiles, solvent mediated forces and further thermodynamic quantities.

An alternative method for obtaining radial distribution functions is via Percus' test particle method [21]. Here one solves for the equilibrium density profiles in the presence of an external potential that represents a test particle located at the origin. It can be shown that these profiles, when normalized by the bulk density, are the radial distribution functions. This is a generally more involved method, as it requires one to implement a numerical solver for the Euler–Lagrange equations for minimizing the functional and hence to calculate inhomogeneous equilibrium density profiles. Such results are expected to be more accurate at small and intermediate distances than those from the OZ route. In [16] Ayadim and Amokrane calculated the $g_{ij}(r)$ using Percus' test particle approach and found good agreement when comparing to Monte Carlo (MC) simulation data. However, the authors also reported that their radial density profiles contained small unphysical jumps due to what they suspected were deficiencies in the construction of the functional.

In order to re-address this issue, in the present paper we calculate the $g_{ij}(r)$ from the NAHS functional. We use both the OZ and the test particle method and compare the respective results to new MC simulation data. For all values of positive and small values of negative non-additivity, we show that the radial distribution functions from the two methods compare well to the simulation results. For strongly negative non-additivity the accuracy of the two methods strongly diverges from the simulation results. Although both theoretical approaches fail at very small values of non-additivity the test particle results show significantly better behaviour than those from the OZ method.

We have previously shown that correlation functions for NAHS mixtures with positive non-additivity exhibit either monotonic asymptotic decay or one of two types of damped oscillatory asymptotic decay with different wavelengths [15]. Here we show that in mixtures with negative non-additivity only the two types of oscillatory decay remain. We investigate the asymptotic decay of the $g_{ij}(r)$ from the test particle method and show that this agrees with that found analytically, for both positive and negative non-additivity. We also investigate strongly negative non-additive mixtures, which start to decouple into two independent pure hard sphere fluids. Here the functional begins to break down, and we show that the test particle method still gives good qualitative agreement but poor quantitative agreement with the MC results.

The paper is organized as follows. In section 2 we give a brief introduction to DFT and to the NAHS functional, in particular we give details about our implementation of the test particle procedure. In section 3 we present results for the radial distribution functions and their asymptotic decay. Finally, in section 4 we draw conclusions.

2. Density functional theory

2.1. The NAHS excess free energy functional

The NAHS pair potential between particles of species i and j is

$$v_{ij}(r) = \begin{cases} \infty & r < \sigma_{ij} \\ 0 & \text{otherwise,} \end{cases} \quad (1)$$

where r is the radial distance between the two particles, σ_{ii} is the diameter of species $i = 1, 2$, and

$$\sigma_{12} = \frac{1}{2}(1 + \Delta)(\sigma_{11} + \sigma_{22}) \quad (2)$$

is the hard core distance between species 1 and 2, where $\Delta \geq -1$ measures the degree of non-additivity. The mixture is parameterized by the ratio of particle diameters, $q = \sigma_{11}/\sigma_{22} \leq 1$, and by Δ . We characterize bulk states by the bulk packing fractions $\eta_i = \pi \rho_i^b \sigma_{ii}^3 / 6$, where ρ_i^b is the bulk number density of species $i = 1, 2$.

For a two-component system the grand potential functional depends on the one-body density profiles, $\rho_i(\mathbf{r})$, where $i = 1, 2$ labels the species, and is given by

$$\Omega[\rho_1, \rho_2] = F_{\text{id}}[\rho_1, \rho_2] + F_{\text{ex}}[\rho_1, \rho_2] - \sum_{i=1}^2 \int d\mathbf{r} \rho_i(\mathbf{r})(\mu_i - V_i(\mathbf{r})) \quad (3)$$

where $F_{\text{id}}[\rho_1, \rho_2] = \sum_{i=1}^2 \int d\mathbf{r} \rho_i(\mathbf{r})(\ln(\Lambda_i^3 \rho_i(\mathbf{r})) - 1)$ is the ideal Helmholtz free energy functional for a binary mixture, Λ_i is the de Broglie wavelength of species i , μ_i is the chemical potential of species i , $V_i(\mathbf{r})$ is the external potential that acts on species i , and \mathbf{r} is the spatial coordinate. The interactions between the particles are described by the excess Helmholtz free energy functional, $F_{\text{ex}}[\rho_1, \rho_2]$, for which an approximation must be used in order to proceed.

The excess Helmholtz free energy functional for NAHSs [14] is a generalization of the fundamental measure theory for additive hard sphere mixtures [22–25], and is built from a set of eight weighted densities, four for each species, $n_{i,\gamma}(\mathbf{r})$, where $\gamma = 0, 1, 2, 3$, which are, in turn, formed from a set of eight weight functions, $w_{i,\gamma}(r)$, convolved with the density profiles,

$$n_{i,\gamma}(\mathbf{x}) = \int d\mathbf{r} \rho_i(\mathbf{r}) w_{i,\gamma}(\mathbf{r} - \mathbf{x}), \quad (4)$$

for $i = 1, 2$. The weighted densities are combined into sixteen ansatz functions for the free energy density, $\Phi_{\alpha\beta}(\{n_{1,\nu}(\mathbf{x})\}, \{n_{2,\tau}(\mathbf{x}')\})$, $\alpha, \beta = 0, 1, 2, 3$, which are then convolved with a set of kernel functions, $K_{\alpha\beta}(r)$, to take account of the non-locality between species 1 and 2. Hence

$$F_{\text{ex}}[\rho_1, \rho_2] = \int \int d\mathbf{x} d\mathbf{x}' \sum_{\alpha,\beta=0}^3 K_{\alpha\beta}(\mathbf{x} - \mathbf{x}') \Phi_{\alpha\beta}(\mathbf{x}, \mathbf{x}'). \quad (5)$$

The details of the NAHS functional, including the form of the weight functions, $w_{i,\gamma}(r)$, of the kernel functions, $K_{\alpha\beta}(r)$, and of the free energy density terms, $\Phi_{\alpha\beta}(\mathbf{x}, \mathbf{x}')$, can be found elsewhere [15].

In order to calculate one-body density profiles, one takes the functional derivative of the grand potential, $\Omega[\rho_1, \rho_2]$, with respect to the density profiles, $\rho_i(\mathbf{r})$. Setting the result to zero [26, 27] yields two Euler–Lagrange equations,

$$\frac{\delta \Omega[\rho_1, \rho_2]}{\delta \rho_i(\mathbf{r})} = k_B T \ln(\Lambda^3 \rho_i(\mathbf{r})) - k_B T c_i^{(1)}(\mathbf{r}) - \mu_i + V_i(\mathbf{r}) = 0, \quad (6)$$

where

$$c_i^{(1)}(\mathbf{r}) = -(k_B T)^{-1} \frac{\delta F_{\text{ex}}[\rho_1, \rho_2]}{\delta \rho_i(\mathbf{r})} \quad (7)$$

is the one-body direct correlation function (of species i), defined via the first functional derivative of the excess Helmholtz free energy functional. The Euler–Lagrange equations (6) for $i = 1, 2$ must be solved simultaneously and self-consistently to obtain the equilibrium profiles, which minimize (3).

Thus, in practice, the key quantity for calculating density profiles is $c_i^{(1)}(r)$, cf (6) and (7). For the present functional calculating this is facilitated by first obtaining a set of intermediate basis functions of the form

$$H_{i,\gamma}(\mathbf{x}) = (k_B T)^{-1} \sum_{\alpha,\beta=0}^3 \int d\mathbf{x}' \phi_{i,\alpha\beta\gamma}(\mathbf{x}, \mathbf{x}') K_{\alpha\beta}(|\mathbf{x} - \mathbf{x}'|), \quad (8)$$

where

$$\phi_{i,\alpha\beta\gamma}(\mathbf{x}, \mathbf{x}') = \frac{\partial \Phi_{\alpha\beta}(\{n_{1,v}\}, \{n_{2,\tau}\})}{\partial n_{i,\gamma}} \quad (9)$$

are derivatives of the free energy terms that depend on \mathbf{x} and \mathbf{x}' via $n_{1,v}(\mathbf{x})$ and $n_{2,\tau}(\mathbf{x}')$, respectively, and depend on species i via the derivative on the right-hand side. The intermediate basis functions (8) are then convolved with the weight functions to give four different contributions to the one-body direct correlation functions,

$$c_{i,\gamma}^{(1)}(\mathbf{r}) = \int d\mathbf{x} w_{i,\gamma}(|\mathbf{x} - \mathbf{r}|) H_{i,\gamma}(\mathbf{x}), \quad (10)$$

which are then summed to give the one-body direct correlation functions, i.e.

$$c_i^{(1)}(\mathbf{r}) = \sum_{\gamma=0}^3 c_{i,\gamma}^{(1)}(\mathbf{r}). \quad (11)$$

The intermediate basis functions (8) have no stand-alone physical significance, at least as far as we can tell. However, monitoring their behaviour can be a vital aspect in checking the accuracy of the implementation of $c_i^{(1)}(\mathbf{r})$ and hence of the Euler–Lagrange equations.

Summarizing, the calculation of $c_i^{(1)}(\mathbf{r})$ requires three steps:

- (1) calculating the weighted densities, (4);
- (2) combining the weighted densities into the analytic expressions $\phi_{i,\alpha\beta\gamma}(\mathbf{x}, \mathbf{x}')$ and convolving these with the kernel weight functions, (8);
- (3) convolving $H_{i,\gamma}(\mathbf{x})$ with $w_{i,\gamma}(\mathbf{x})$ and summing over γ , (10) and (11).

Steps 1 and 3 are simple convolutions and can be performed both in planar and in spherical geometry using fast Fourier transforms. The convolutions in equation (8) reduce a function of the two spatial arguments \mathbf{x}, \mathbf{x}' to a function of a single space point, and furthermore the kernels $K_{\alpha\beta}(r)$ have a very small range compared to the size of the density profiles (i.e. the total length of the numerical grid). Therefore, we found it to be more efficient to perform these convolutions via direct real space integration, such that only the values of $\phi_{i,\alpha\beta\gamma}(\mathbf{x}, \mathbf{x}')$ that are actually required are calculated.

In order to reduce potential sources of error when performing and transcribing the derivatives $\partial \Phi_{\alpha\beta} / \partial n_{i,\gamma}$ we have obtained these analytic expressions via computational

symbolic differentiation and then converted the expressions into source code for the numerics. However, one must still correctly implement all kernel functions $K_{\alpha\beta}(r)$.³

For planar geometry (see e.g. [15]) the kernel convolutions are of the form

$$H_{i,\alpha\beta\gamma}(z) = \int dz' \phi_{i,\alpha\beta\gamma}(z') \bar{K}_{\alpha\beta}(z - z'), \quad (12)$$

where $H_{i,\alpha\beta\gamma}(z)$ are the individual components of the intermediate basis functions (8), z is the planar distance and

$$\bar{K}_{\alpha\beta}(z) = 2\pi \int_0^\infty d\xi \xi K_{\alpha\beta}(\sqrt{\xi^2 + z^2}) \quad (13)$$

are the integrated (planar) kernel functions described in the appendix of [15]; these have a range $R_{12} = \Delta(\sigma_{11} + \sigma_{22})/2$. For spherical geometry, provided that $r > R_{12}$, the convolutions are very similar:

$$H_{i,\alpha\beta\gamma}(r) = \frac{1}{r} \int dr' r' \phi_{i,\alpha\beta\gamma}(r') \bar{K}_{\alpha\beta}(|r - r'|), \quad (14)$$

where r is the radial distance, and the integrated kernel functions are identical to those in the planar case. Thus, the form of the integrated kernel functions remains the same as in the planar case and provided that $r > R_{12}$ the only difference is the inclusion of a term r'/r in the spherical convolutions.

2.2. Two routes to radial distribution functions

Percus' test particle approach [21] rests on calculating inhomogeneous density profiles in the presence of a single particle. The key is to set the external potential in (6) such that it represents a single 'test' particle located at the origin, i.e.

$$V_i(\mathbf{r}) = v_{ij}(r), \quad j = 1, 2, \quad (15)$$

where $r = |\mathbf{r}|$, and $v_{ij}(r)$ are the pair potentials, here defined by equation (1). It can be shown that the equilibrium one-body profile in the presence of this external potential is proportional to the two-body (partial) pair correlation function, i.e. $\rho_i(r)/\rho_i^b = g_{ij}(r)$, where ρ_i^b is the bulk density of species i and $\rho_i(r)$ is the solution of (6). For a binary mixture the calculation must be repeated twice, since a particle of either species must be located at the origin. Using this method we calculate $g_{ij}(r)$ for the NAHS model, and will refer to this as the test particle route.

In [15] we used the alternative route for calculating $g_{ij}(r)$, i.e. via the OZ equation,

$$h_{ij}(r) = c_{ij}^{(2)}(r) + \sum_{l=1}^2 \rho_l^b \int d\mathbf{r}' h_{il}(r') c_{lj}^{(2)}(|\mathbf{r} - \mathbf{r}'|), \quad (16)$$

where $h_{ij}(r) = g_{ij}(r) - 1$ is the total correlation function, and $c_{ij}^{(2)}(r)$ is the two-body direct correlation function. In the DFT

³ Checking numerically their remarkable algebraic group structure [32, 33] could be a further valuable test in developing and debugging numerical codes.

context this is defined by taking a second functional derivative of $F_{\text{ex}}[\rho_1, \rho_2]$,

$$c_{ij}^{(2)}(|\mathbf{r} - \mathbf{r}'|) = -(k_B T)^{-1} \left. \frac{\delta^2 F_{\text{ex}}[\rho_1, \rho_2]}{\delta \rho_i(\mathbf{r}) \delta \rho_j(\mathbf{r}')} \right|_{\rho_1, \rho_2 = \text{const}}. \quad (17)$$

For the present functional analytic expressions for the Fourier representations of the direct and total correlation functions, $\hat{c}_{ij}^{(2)}(k)$ and $\hat{h}_{ij}(k)$, can be obtained via equation (16), where k is the argument in Fourier space. By numerically Fourier transforming one can then obtain $h_{ij}(r)$. We will henceforth refer to this method as the OZ route. We use this method here to calculate the radial distribution functions and also investigate their different types of asymptotic decay.

3. Results

3.1. Radial distribution functions

We have calculated radial distribution functions for a range of size ratios and both positive and negative values of the non-additivity parameter Δ . As a representative example, we first return to the case featured in both [14] and [16], where the model parameters are $q = 0.5$ and $\Delta = 0.3$, and statepoint $\eta_2 = 0.1$ and $\eta_1 = \eta_2/8$ [28]⁴. We refer to this set of parameters as statepoint A. In figure 1(a) we show the $g_{ij}(r)$ calculated using the OZ and test particle methods. Although the OZ route fails to correctly reproduce the core condition $g_{ij}(r < \sigma_{ij}) = 0$, the correlation functions agree well both at contact and for larger distances.

In order to test the accuracy of the NAHS functional we have carried out MC simulations to obtain reference data for $g_{ij}(r)$. We performed canonical simulations for a mixture of 1024 particles divided equally between the two species. We used 10^5 MC moves per particle for equilibration, and 10^6 moves per particle for data collection. The MC results are plotted in figure 1 and show that, as described in [14, 16], there is good agreement between the OZ and the test particle approach and the simulations.

However, we do not find evidence of the unphysical jumps described in [16] for these parameters. To illustrate the smoothness of our results and to also shed some light on the internal workings of the functional, in figures 1(b) and (c) we plot the intermediate, $H_{i,\gamma}(r)$, and final contributions, $c_{i,\gamma}^{(1)}(r)$, to the (inhomogeneous) one-body direct correlation function for species 2, $c_2^{(1)}(r)$, around a particle of species 1. The intermediate functions, $H_{i,\gamma}(r)$, are not necessarily smooth functions, but rather exhibit features dictated by their order, γ . Namely, $H_{i,0}(r)$ is smooth, $H_{i,1}(r)$ exhibits abrupt changes in the gradient, $H_{i,2}(r)$ exhibits steps (Heaviside functions), and $H_{i,3}(r)$ exhibits sharp spikes (Dirac delta functions). However, we find that when these functions are convolved with the corresponding weight functions, $w_{i,\gamma}(r)$, to produce the $c_{i,\gamma}^{(1)}(r)$, which form the elements of the direct correlation functions via (11), all discontinuities are smoothed out and disappear.

⁴ The correct values used for figure 1 of [16] are those given in the text, not $\eta_2 = 0.05$ and $\eta_1 = \eta_2/8$, as indicated in [16].

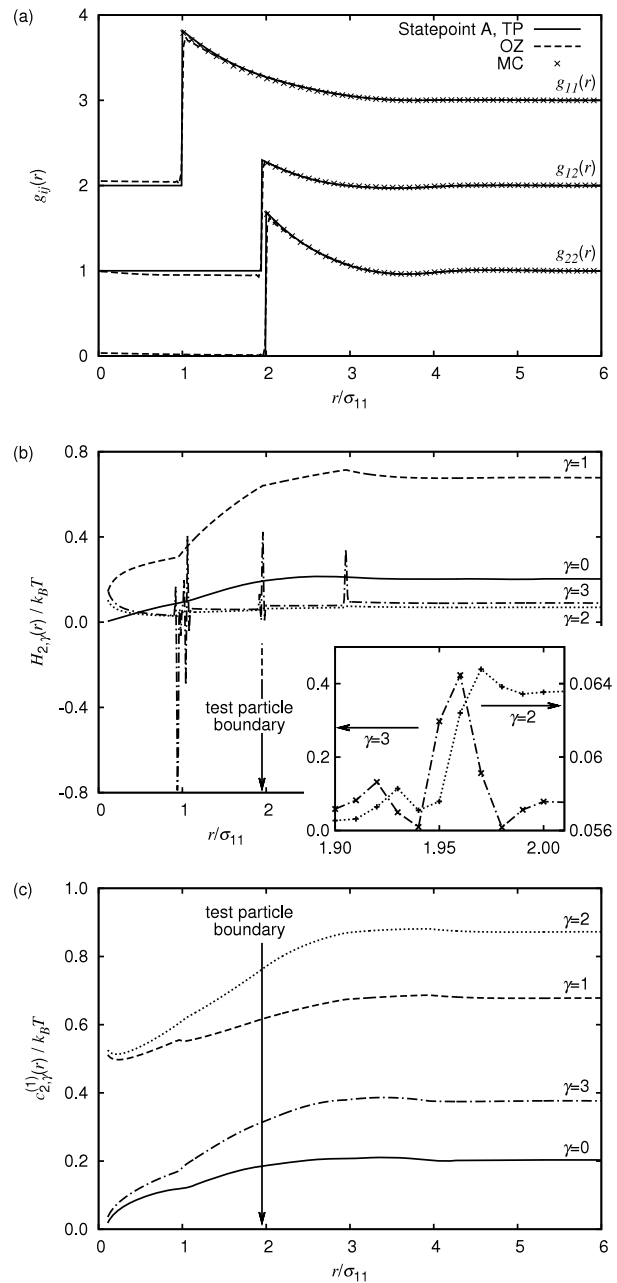


Figure 1. (a) Radial distribution functions, $g_{ij}(r)$, as a function of the scaled distance r/σ_{11} for $q = 0.5$, $\Delta = 0.3$, at statepoint A, $\eta_2 = 0.1$ and $\eta_1 = \eta_2/8$. Shown are results from the test particle route (TP, solid line), inversion of the OZ equation (OZ, dashed line), and MC simulations (MC, symbols). Curves are offset vertically by one unit for clarity. (b) and (c) show the intermediate, $H_{i,\gamma}(r)$, and final contributions, $c_{i,\gamma}^{(1)}(r)$, to the one-body direct correlation function for species $i = 2$, calculated around a test particle of species 1. The inset to (b) shows the region at the test particle boundary, highlighting the Heaviside-type features in $H_{2,2}(r)$, and the Dirac-function-like features in $H_{2,3}(r)$. The numerical grid has spacing $0.01 \sigma_{11}$ and the lines within the inset to (b) are a guide to the eye.

Hence the discontinuities within the intermediate terms are smoothed by convolutions with the weight functions. The structure of the functional implies that the order of the discontinuities in the intermediate terms are smoothed by weight functions, which themselves contain discontinuities.

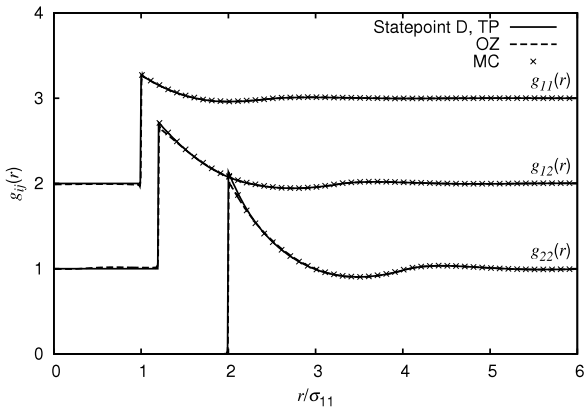


Figure 2. Same as figure 1(a), but for $\Delta = -0.2$ and at statepoint D, $\eta_2 = 0.25$ and $\eta_1 = \eta_2/8$.

For example, $H_{i,3}(r)$, which exhibits spikes, is convolved with $w_{i,3}(r)$, which only has a step, while $H_{i,0}(r)$, which is smooth, is convolved with $w_{i,0}(r)$, which possesses (derivatives of) spikes.

Therefore, we find that each final contribution to $c_i^{(1)}(r)$ is continuous, as seen in figure 1(c). This is even true for the test particle boundary, where the density profiles vary discontinuously due to the hard sphere potential, equation (1). This discontinuous external potential is the origin of the non-smooth features in $H_{i,\gamma}(r)$ that occur at various distances that can be built from (additive) combinations of $\sigma_{ii}/2$, and R_{12} . Nevertheless, we find that $c_i^{(1)}(r)$ is continuous at all distances r .

We have used the virial theorem to calculate the bulk pressure p via $p/(\rho k_B T) = 1 + (2\pi\rho/3) \sum_{ij} x_i x_j \sigma_{ij}^3 g_{ij}(\sigma_{ij}^+)$, where $\rho = \rho_1 + \rho_2$ is the total density, $x_i = \rho_i/\rho$ is the mole fraction of species $i = 1, 2$, and $g_{ij}(\sigma_{ij}^+)$ is the contact value of the partial pair correlation function between species i and j . The case shown in figure 1 is characterized by $x_1 = x_2 = 0.5$, $\rho\sigma_{11}^3 = 0.0477465$, $\sigma_{12}/\sigma_{11} = 1.95$, and $\sigma_{22}/\sigma_{11} = 2$. We analyse the contact values from the test particle calculation. When fixing a small (species 1) particle, $g_{11}(\sigma_{11}^+) = 1.82080$ and $g_{21}(\sigma_{12}^+) = 1.2859$. For a large (species 2) particle fixed at the origin, $g_{12}(\sigma_{12}^+) = 1.3017$ and $g_{22}(\sigma_{22}^+) = 1.6934$. The virial theorem then yields for the (scaled) pressure $p\sigma_{11}^3/(k_B T) = 0.08899$. This is to be compared to the result obtained from the derivative of the bulk free energy F with respect to volume V , where we obtain $(\sigma_{11}^3/k_B T) \partial F/\partial V = 0.08984$. The agreement of both values is within a relative error of 1%, which indicates the good internal consistency of the theory. Note further that the contact values given above satisfy the sum rule $g_{12}(\sigma_{12}^+) = g_{21}(\sigma_{12}^+)$ to within a relative error of 1.2%.

We have also calculated $g_{ij}(r)$ for negative values of Δ using the OZ and the test particle approaches, and compared to results from MC simulation. We find that the level of agreement depends strongly on the degree of non-additivity; for small negative values of Δ , we find that there is good agreement between the three approaches. In figure 2 we plot results for $q = 0.5$, and relatively small negative non-additivity, $\Delta = -0.2$, for partial bulk packing fractions $\eta_2 = 0.25$ and $\eta_1 = \eta_2/8$. We refer to this as statepoint D. We find that there is very good agreement between the three

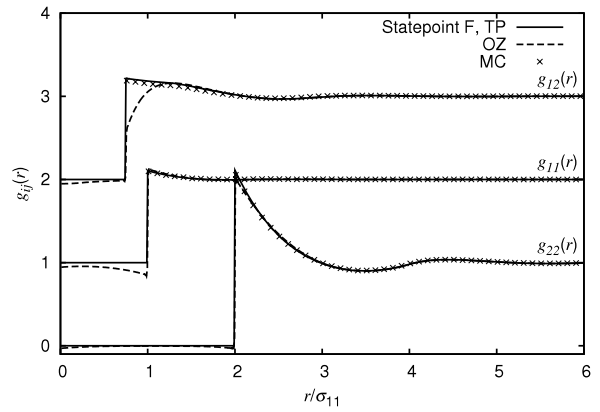


Figure 3. Same as figure 1(a), but for $\Delta = -0.5$ and at statepoint F, $\eta_2 = 0.25$ and $\eta_1 = \eta_2/8$. Note that the curves are plotted in a different order compared to figures 1(a) and 2.

approaches, with the only noticeable differences occurring very close to contact.

However, as Δ is decreased, differences become apparent. In figure 3 we plot results for a stronger negative case, $q = 0.5$, $\Delta = -0.5$, at the same partial packing fraction $\eta_2 = 0.25$ and $\eta_1 = \eta_2/8$ (statepoint F). We find that the three approaches still agree well for the like-like pair correlation functions, but for the unlike case there are clear differences. The OZ route predicts a completely unphysical downturn close to contact [29]. The direct correlation functions (not shown) possess corresponding abnormal features, e.g. the cross correlation function violates the Percus–Yevick approximation $c_{12}(r > \sigma_{12}) = 0$, and develops a (small) tail outside of the core. Furthermore, in the limit $\Delta \rightarrow -1$ (and hence $\sigma_{12} \rightarrow 0$), the functional does not correctly decouple the mixture into two independent hard sphere fluids. On the other hand, as shown in figure 3, the test particle result only slightly overestimates the unlike correlation function close to contact, as compared to the MC results. We explore the strongly negative case in more detail below.

3.2. Asymptotic decay of correlations

It can be shown [17] for systems with short range interaction potentials, that the OZ equations can be transformed so that the radial distribution functions are given by a sum over the poles (divergences) of the partial structure factors,

$$r h_{ij}(r) = \sum_n A_{ij,n} \exp(ik_n r) \quad (18)$$

where i is the imaginary unit, $k_n = \alpha_1 + i\alpha_0$ is the complex position of the n th pole, i.e. where the partial structure factors $S_{ij}(k) = \delta_{ij} + \sqrt{\rho_i^b \rho_j^b} \hat{h}_{ij}(k)$ satisfy

$$S_{ij}^{-1}(k_n) = 0, \quad (19)$$

with α_1 being the real part and α_0 being the imaginary part, and $A_{ij,n}$ the residue of the pole. There is an infinite number of poles, which either occur in conjugate complex pairs, $k_n = \pm\alpha_1 + i\alpha_0$, or as a single purely imaginary pole, $k = i\alpha_0$.

The purely imaginary pole gives a monotonically decaying contribution, $\exp(-\alpha_0 r)/r$, to $h_{ij}(r)$. The complex conjugate pairs give rise to oscillatory contributions to $h_{ij}(r)$, $\cos(\alpha_1 r - \theta_{ij}) \exp(-\alpha_0 r)$, where θ_{ij} is a phase. In both cases, the decay length α_0^{-1} , and the oscillatory wavelength α_1^{-1} are the same for all correlation functions, i.e. independent of the combination of i, j .

The advantage of this method is that it is possible to investigate individual contributions to the radial distribution functions. However, it is usually impractical to investigate the contribution from every pole. It is far more useful to identify the contributions with the smallest imaginary parts, i.e. the poles with the smallest α_0 . These have the largest decay length, and determine the asymptotic (large r) decay of the correlation functions.

As the model parameters and statepoint change, the asymptotic decay can change abruptly from monotonic to oscillatory, or between two oscillatory types with differing wavelengths. The line that divides the regions of monotonic decay from the oscillatory region is known as the Fisher–Widom line [17], and the line between two types of oscillatory decay is known as a structural crossover line, following Grodon *et al* [30].

In [15] we investigated the asymptotic, $r \rightarrow \infty$, decay of $g_{ij}(r)$ and showed that for mixtures with $q = 0.5$ with positive non-additivity, depending on the statepoint, there are three different types of asymptotic decay: two with damped oscillatory decay with different wavelengths corresponding to the diameters, σ_{ii} , of the particles, and a third type, where the correlations decay monotonically. In the phase diagram the regions of different decay in relation to the fluid–fluid demixed region can be indicated (see e.g. figures 9 and 12 for $\Delta = 0.1$ in [4]).

Here we investigate the asymptotic decay of the correlation functions, $g_{ij}(r)$, from the test particle calculations and compare to the analytical pole analysis. Therefore, we have performed the pole analysis to deduce the type of asymptotic correlations for the same parameters as shown in figure 1, i.e. $q = 0.5$ and $\Delta = 0.3$. Figure 4 shows the corresponding fluid–fluid demixing phase diagram, including the binodal, spinodal and bulk critical point. We indicate the three regions with different types of asymptotic decay, separated by the Fisher–Widom and structural crossover lines. We find that the phase diagram is dominated by two of the regions; one where the oscillatory wavelength is similar to the diameter of the larger species, σ_{22} , (labelled Osc₂) and one where the decay is monotonic (labelled Mono). The second oscillatory region (Osc₁), with a wavelength similar to the smaller species, σ_{11} , is very small and lies very close to the η_1 -axis, see the inset to figure 4 for a zoom of the region close to the η_1 -axis.

We find that the statepoint considered in figure 1, marked in the phase diagram as statepoint A, lies within the Osc₂ region. For comparison, we choose two further statepoints that reside in the other regions of asymptotic decay, which are marked statepoints B and C; these lie in the Osc₁ and Mono regions, respectively. We show the partial pair correlation functions calculated for statepoints B and C in figure 5(a).

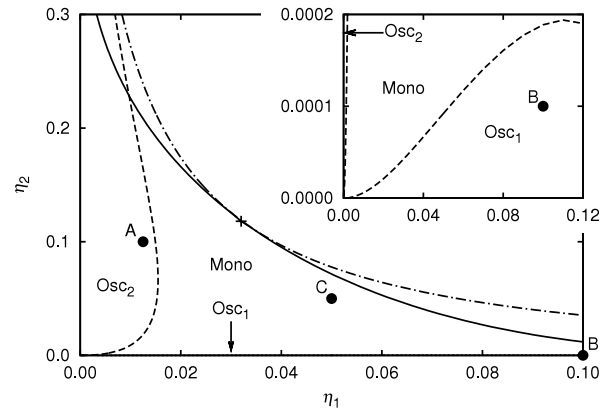


Figure 4. Fluid–fluid demixing phase diagram for $q = 0.5$, and $\Delta = 0.3$. The binodal (solid line) and spinodal (dash-dotted line) for fluid–fluid demixing meet at the bulk critical point (+). The asymptotic decay of the correlation functions, $h_{ij}(r)$, is either monotonic (Mono), or exhibits oscillations (Osc₁ and Osc₂). The labels A, B and C indicate statepoints for which the correlation functions are shown in figure 5.

Although there are some differences between these results and those presented for statepoint A in figure 1, the type of asymptotic decay is not apparent on a linear scale. To elucidate the asymptotic decay in figure 5(b), we plot $\ln(|rh_{ij}(r)|)$ for the three statepoints marked in figure 4; recall that $h_{ij}(r) = g_{ij}(r) - 1$ are the total correlation functions.

We observe that for statepoint A the decay is indeed oscillatory, and that the wavelength is of the order of the diameter of the bigger particles. The region to the right of the figure, $r \simeq 10\sigma_{11}$, is where the departure of the profiles from the bulk value approaches the accuracy of the numerical representation. The correlations at statepoint B are also oscillatory, but with a much smaller wavelength, approximately half that found for statepoint A. Furthermore, the oscillations decay very quickly, so that the results reach the level of numerical accuracy at $r \simeq 6\sigma_{11}$. The correlations for statepoint C decay monotonically and since this statepoint is also close to the coexistence region, the decay is very slow.

We next investigate the asymptotic behaviour of the pair correlation functions for negative Δ , which has not been addressed before. Consistent with the fact that the NAHS fluid with negative non-additivity does not show fluid–fluid phase separation, we find that the asymptotic decay is always oscillatory, but either with a wavelength corresponding to the bigger or to the smaller particles. This scenario is the same as that found within a DFT framework for additive hard spheres [30]. In figure 6(a) we plot the phase diagram for $q = 0.5$ and $\Delta = -0.2$, again labelling these two regions Osc₁ and Osc₂. We find that the statepoint corresponding to the results shown in figure 2 lies in the Osc₂ region and label this statepoint D. We also choose a further statepoint which is within the Osc₁ region, labelled statepoint E. The profiles calculated using the test particle method corresponding to this statepoint are shown in figure 6(b). We find that the like–like correlation function for the larger particles (which constitute the minority species) does not exhibit a local maximum at

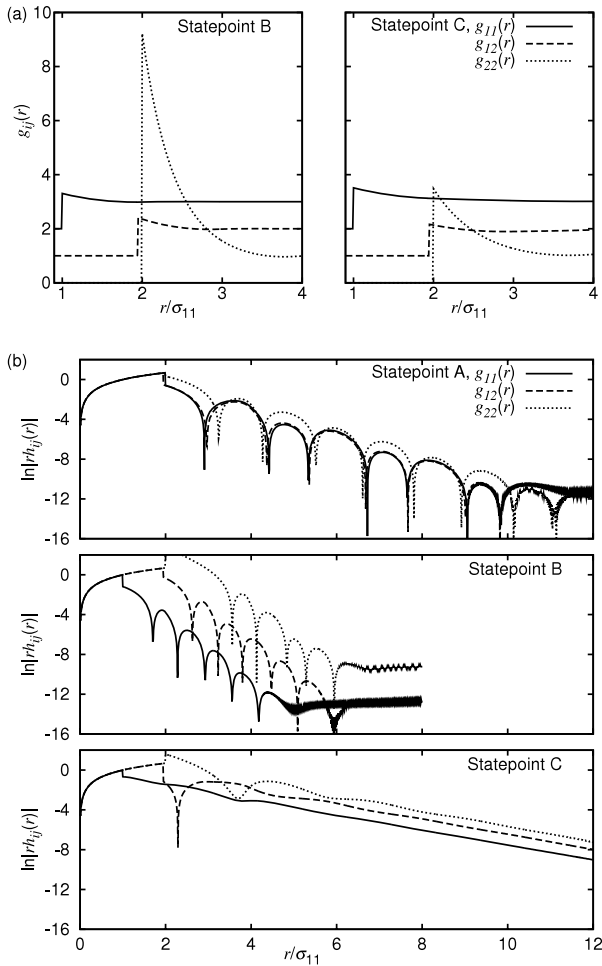


Figure 5. (a) Radial distribution functions obtained from the test particle route for parameters $q = 0.5$, and $\Delta = 0.3$ at statepoints B and C, as shown in figure 4. (b) Total correlation functions, $h_{ij}(r) = g_{ij}(r) - 1$ plotted as $\ln|r h_{ij}(r)|$, for statepoints A, B and C. The asymptotic decay for statepoints A and B is oscillatory. For statepoint A the wavelength is similar to the diameter of the bigger species σ_{22} , and for statepoint B it is similar to the diameter of the smaller species, σ_{11} . For statepoint C all correlation functions decay monotonically.

contact, and that the maximum in the correlation function occurs at $r \simeq 2.5\sigma_{11}$. In order to test these results we have carried out further MC simulations using a total of 5000 particles, 88 of which are species 2, and plotted these results alongside the test particle curves. We find that $g_{11}(r)$ and $g_{12}(r)$ from the two approaches agree very well. However, for $g_{22}(r)$ the test particle method does underestimate the value at contact, although because of the relatively small number of big particles the MC statistics are poorer. In figure 6(b) we plot the asymptotic decay of $g_{ij}(r)$ at statepoints D and E. We find that both appear oscillatory, but that the oscillatory wavelength in D is approximately twice that of statepoint E, as expected from the pole analysis.

3.3. Symmetric mixtures with negative non-additivity

We return to mixtures with negative Δ . We previously showed, in figure 3, that for negative $\Delta \simeq -0.5$ the OZ route predicts

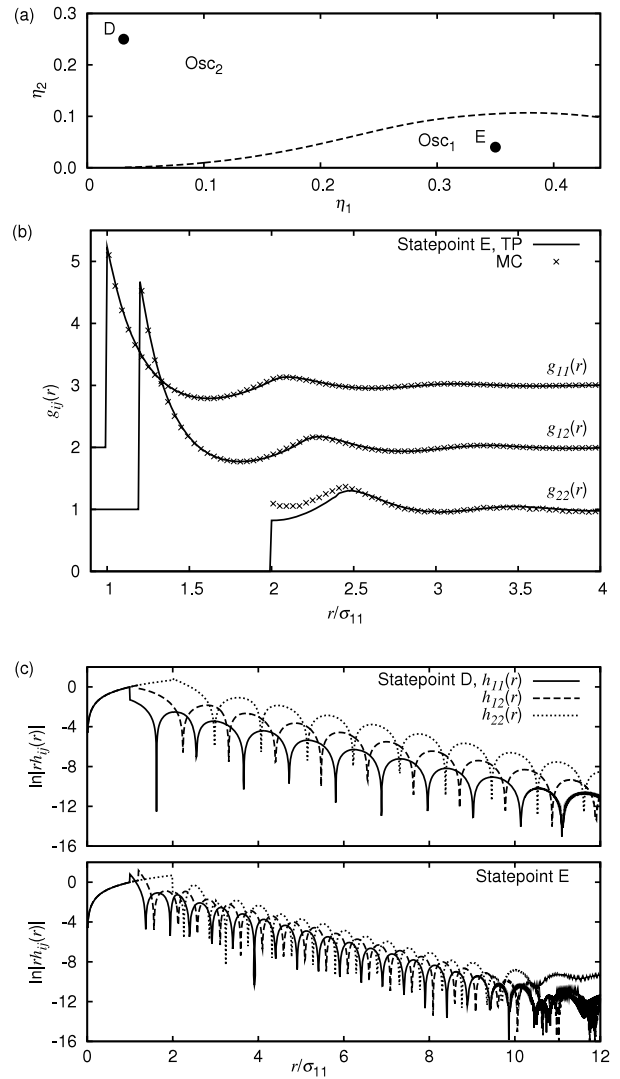


Figure 6. (a) Regions of different asymptotic decay in the η_1, η_2 plane for $q = 0.5$ and $\Delta = -0.2$. Since Δ is negative, the mixture does not show fluid phase separation. There are only two types of asymptotic decay, both oscillatory, but with different wavelengths. (b) The partial pair distribution functions at statepoint E calculated from the test particle (TP, line) and MC (symbols) approaches. For $g_{22}(r)$ both approaches indicate stronger correlations at $r \simeq 2.5\sigma_{11}$ than at contact. (c) The asymptotic decay of the correlation functions for statepoints D and E, showing oscillatory decay for both statepoints but with different wavelengths.

an unphysical downturn of the unlike correlation functions near contact [29]. We have found that this is also true for values of Δ below -0.5 and therefore we conclude that the OZ route is not well suited to study such conditions. However, it is still interesting to investigate the agreement between results from the test particle route and from MC. For simplicity we restrict ourselves to the symmetric size ratio, $q = 1$, and slowly decrease Δ from 0. We do this at a high overall density with an equal packing fraction of both species, $\eta_1 = \eta_2 = 0.25$. In figure 7 we plot $g_{ij}(r)$ from the test particle route, and the MC results for $\Delta = -0.1, -0.2, -0.3, -0.4$, and -0.5 .

We find that at this considerably high density there is reasonably good agreement between the simulation and test

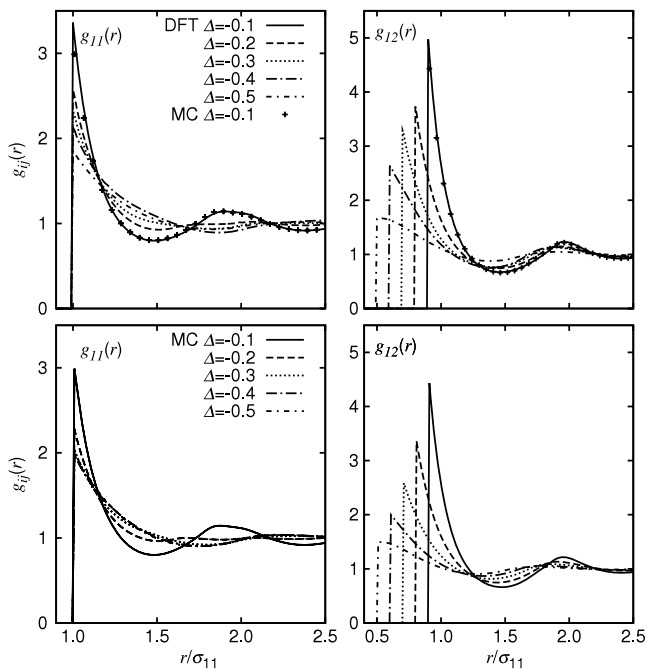


Figure 7. Series of $g_{11}(r)$ (left) and $g_{12}(r)$ (right) for $q = 1$, $\eta_1 = \eta_2 = 0.25$, and varying $\Delta = -0.1, -0.2, -0.3, -0.4, -0.5$ (as indicated). The two top panels show the results from the DFT, and the two bottom panels those from simulations. For $\Delta = -0.1$ the simulation results (symbols) are also directly compared to the DFT results in the top panels. The simulation results show that for $\Delta \lesssim -0.3$ the like-like correlation function, $g_{11}(r)$, almost does not vary with Δ but becomes essentially that of a pure hard sphere fluid.

particle results only for $\Delta = -0.1$. For lower values of Δ , although the general behaviour of the partial pair correlation functions is correctly predicted by the test particle route, there are, however, significant quantitative deviations from the MC data. Within the simulations we find that for $\Delta \lesssim 0.3$ results for $g_{11}(r)$ change very little with Δ and become essentially equal to the pair correlation function of a pure hard sphere fluid at packing fraction $\eta = 0.25$. Meanwhile, $g_{12}(r)$ continues to change with decreasing Δ , losing all structure as the two species cease to interact. Note that in the extreme case $\Delta = -1$, the two species decouple and strictly $g_{12}(r) = 1$.

4. Conclusions

In conclusion, we have investigated the partial radial distribution functions of non-additive hard sphere mixtures with positive or negative non-additivity using MC simulations, as well as two different DFT approaches, one based on the OZ and the other on Percus' test particle method. We have shown that for positive values of Δ there is good agreement between the results from simulations and both DFT methods. Depending on the density, for small negative values of $\Delta \simeq -0.1$ or 0.2 , we find that there is again good agreement between the three approaches. However, for more negative values of Δ the OZ route exhibits unphysical features, whilst the test particle result still gives a reasonably good account of the bulk structure of the NAHS mixture. For very low negative values of Δ the test particle results are only qualitatively

correct, and show very poor numerical agreement with the MC data. For $\Delta \neq 0$ the OZ route does not reproduce the core condition. Whether the functional can be modified in order to improve the situation is an interesting question for future work. We have also investigated the asymptotic (large distance) decay of the correlation functions and shown that the asymptotic decay of the test particle results agrees with the prediction of the analytical pole analysis.

In all cases we find that the test particle results for the density profiles do not exhibit any unphysical jumps. From our own experience artefacts such as those reported in an earlier study [16] can easily occur due to incorrect implementation of the functional. The present density functional includes a large number of terms that contribute and of convolutions that need to be carried out. Hence small errors in the implementation can cause subtle errors in otherwise correct profiles. We conclude that the NAHS functional is free of artefacts in both planar and spherical implementations and that the functional does not require fundamental modifications as suggested in [16]. In the present paper we have described some of the computational methods that we used, in particular using symbolic algebra to correctly implement the free energy derivative terms.

We have therefore shown that the NAHS functional is very reliable for the prediction of the pair structure of the bulk fluid for both positive and small negative values of Δ . This suggests that in future work the binary NAHS functional could be used as a reference to be augmented by more complicated interactions including attractive and repulsive short range tails [31], long ranged electro-static interactions treated with a Poisson-Boltzmann approach [10, 11], or modelling polymeric systems [12, 13]. Furthermore, the DFT could be used in Oettel's general reference functional approach [34].

After completion of this work we learnt that the authors of [16] detected the origin of the subtle numerical artefacts [28].

Acknowledgments

We thank Martin Oettel for useful discussions and for communicating his results for the partial pair correlation functions to us. We thank Said Amokrane and Abderrahime Ayadim for useful correspondence. We gratefully acknowledge the EPSRC for funding under grant EP/E06519/1 and the SFB 840/A3 of the DFG.

References

- [1] Kahl G 1990 *J. Chem. Phys.* **93** 5105
- [2] Ayadim A and Amokrane S 2010 *J. Phys. Chem. B* **114** 16824
- [3] Brunet C, Malherbe J G and Amokrane S 2010 *Phys. Rev. E* **82** 021504
- [4] Hopkins P and Schmidt M 2011 in preparation
- [5] Hopkins P and Schmidt M 2011 *Phys. Rev. E* **83** 050602(R)
- [6] Ballone P, Pastore G, Galli G and Gazzillo D 1986 *Mol. Phys.* **59** 275
- [7] Gazzillo D and Pastore G 1989 *Chem. Phys. Lett.* **159** 388
- [8] Gazzillo D, Pastore G and Frattini R 1990 *J. Phys.: Condens. Matter* **2** 8463

- [9] Paricaud P 2008 *Phys. Rev. E* **78** 021202
- [10] Kalcher I, Horinek D, Netz R and Dzubiella J 2009 *J. Phys.: Condens. Matter* **21** 424108
- [11] Kalcher I, Schulz J C F and Dzubiella J 2010 *J. Chem. Phys.* **133** 164511
- [12] Abu-Sharkh B and Hamad E 2004 *Langmuir* **20** 254
- [13] Malakhov A and Volkov V 2007 *Polym. Sci. A* **49** 745
- [14] Schmidt M 2004 *J. Phys.: Condens. Matter* **16** 351
- [15] Hopkins P and Schmidt M 2010 *J. Phys.: Condens. Matter* **22** 035108
- [16] Ayadim A and Amokrane S 2010 *J. Phys.: Condens. Matter* **22** 035103
- [17] Evans R, Leote de Carvalho R J F, Henderson J R and Hoyle D C 1994 *J. Chem. Phys.* **100** 591
- [18] Evans R, Henderson J R, Hoyle D C, Parry A O and Sabeur Z A 1993 *Mol. Phys.* **80** 755
- [19] Leote de Carvalho R J F, Evans R and Rosenfeld Y 1999 *Phys. Rev. E* **59** 1435
- [20] Evans R and Henderson J R 2009 *J. Phys.: Condens. Matter* **21** 474220
- [21] Percus J K 1962 *Phys. Rev. Lett.* **8** 462
- [22] Tarazona P, Cuesta J A and Martinez-Raton Y 2008 *Lect. Notes Phys.* **753** 247
- [23] Roth R 2010 *J. Phys.: Condens. Matter* **22** 063102
- [24] Rosenfeld Y 1989 *Phys. Rev. Lett.* **63** 980
- [25] Kierlik E and Rosinberg M L 1990 *Phys. Rev. A* **42** 3382
- [26] Evans R 1979 *Adv. Phys.* **28** 143
- [27] Dwandaru W S B and Schmidt M 2011 *Phys. Rev. E* **83** 061133
- [28] Ayadim A and Amokrane S 2011 private communication
- [29] Oettel M 2008 private communication
- [30] Grodon C, Dijkstra M, Evans R and Roth R 2004 *J. Chem. Phys.* **121** 7869
- [31] Schaink H M and Hoheisel C 1992 *J. Chem. Phys.* **97** 8561
- [32] Schmidt M and Jeffrey M R 2007 *J. Math. Phys.* **48** 123507
- [33] Schmidt M 2011 *Mol. Phys.* **109** 1253
- [34] Oettel M 2005 *J. Phys.: Condens. Matter* **17** 429